Random Walk of Processive, Quantum Dot-Labeled Myosin Va Molecules within the Actin Cortex of COS-7 Cells

Shane R. Nelson, M. Yusuf Ali, Kathleen M. Trybus, and David M. Warshaw*
Department of Molecular Physiology and Biophysics, University of Vermont College of Medicine, Burlington, Vermont

ABSTRACT Myosin Va (myoVa) is an actin-based intracellular cargo transporter. In vitro experiments have established that a single myoVa moves processively along actin tracks, but less is known about how this motor operates within cells. Here we track the movement of a quantum dot (Qdot)-labeled myoVa HMM in COS-7 cells using total internal reflectance fluorescence microscopy. This labeling approach is unique in that it allows myoVa, instead of its cargo, to be tracked. Single-particle analysis showed short periods ($\leq$0.5 s) of ATP-sensitive linear motion. The mean velocity of these trajectories was 604 nm/s and independent of the number of myoVa molecules attached to the Qdot. With high time (16.6 ms) and spatial (15 nm) resolution imaging, Qdot-labeled myoVa moved with sequential 75 nm steps per head, at a rate of 16 s^{-1}, similarly to myoVa in vitro. Monte Carlo modeling suggests that the random nature of the trajectories represents processive myoVa motors undergoing a random walk through the dense and randomly oriented cortical actin network.

INTRODUCTION

Cargo transport from the cell center to the periphery involves coordination between microtubule- and actin-based motors. The prevailing view is that kinesin powers long-range movement on microtubules away from the nucleus, followed by a handoff to myosin Va (myoVa) for local delivery within the dense actin cortex (1–3). In vitro studies have established several features of myoVa that may facilitate successful cargo transport within the cell. The ability of myoVa to rapidly diffuse long distances along microtubules with no energy consumption (4,5) would allow it to scan the microtubule and link up with motor-cargo complexes that are being actively transported by kinesin. Once transferred to actin, a single myoVa molecule can move processively for several microns, taking sequential 75 nm steps per head (~36 nm movement of the molecule's center of mass), in a hand-over-hand fashion (6,7). Although the complex actin cytoskeleton may pose a physical challenge to myoVa transport, the motor's structural flexibility allows it to adeptly maneuver through actin-actin intersections and Arp2/3 junctions (4), thus ensuring continuous movement of the cargo to its final destination. None of these features, most importantly myoVa's processivity, have been firmly established to occur within cells.

Kinesin- and dynein-based intracellular organelle movements on microtubules have been inferred from the ~8 nm stepwise movements observed during tracking of fluorescently labeled peroxisomes or endocytosed quantum dot (Qdot)-containing vesicles (8–10). Similarly, 36 nm steps associated with melanosome trafficking have been attributed to myosin V (2,11). Even though these step sizes are consistent with single-motor in vitro data for myoVa (12,13), the observed movement may originate from complex mechanical interactions between multiple motors, both actin- and microtubule-based, that exist on a given cargo (14).

To characterize the motion of single myoVa molecules within a cellular environment and the challenges that are presented by the complex cytoskeletal meshwork, we introduced Qdot-labeled myoVa heavy meromyosin (HMM) by pinocytosis into mammalian COS-7 cells. Qdots offer an advantage over fluorescent dyes in that they are 20 times brighter and resistant to photobleaching, and can be nontoxic to cells for periods of up to several days (15). We took advantage of these fluorescent semiconductor nanocrystals in this study, as in previous studies (4,5,7), to serve as both cargo and a label for single myoVa HMM molecules. With this approach, we were able to use total internal reflectance fluorescence (TIRF) microscopy to directly observe individual myoVa motors as they transported their Qdot cargo within the actin cortex.

Using these techniques, we observed sequential 75 nm steps taken by a single myoV HMM molecule in COS-7 cells, establishing that processive movement occurs within a cell. Single-particle mean-squared displacement (MSD) analysis of the trajectories, along with Monte Carlo model simulations, suggests that the paths reflect the processive motion of a myoVa motor traveling along an effectively random cortical actin network. The rate of movement was the same whether it was measured in vitro and or in the context of the high viscosity of the cytoplasm, and was independent of the number of motors. Our data thus demonstrate that the most basic biophysical properties associated with myoVa transport in vitro—namely, its processivity and ability to navigate actin-actin intersections—are recapitulated within the complex cellular environment.

Submitted February 14, 2009, and accepted for publication April 21, 2009.

*Correspondence: warshaw@physiolgy.med.uvm.edu

Editor: Claudia Veigel.

0006-3495/09/07/0509/10 $2.00

doi: 10.1016/j.bpj.2009.04.052

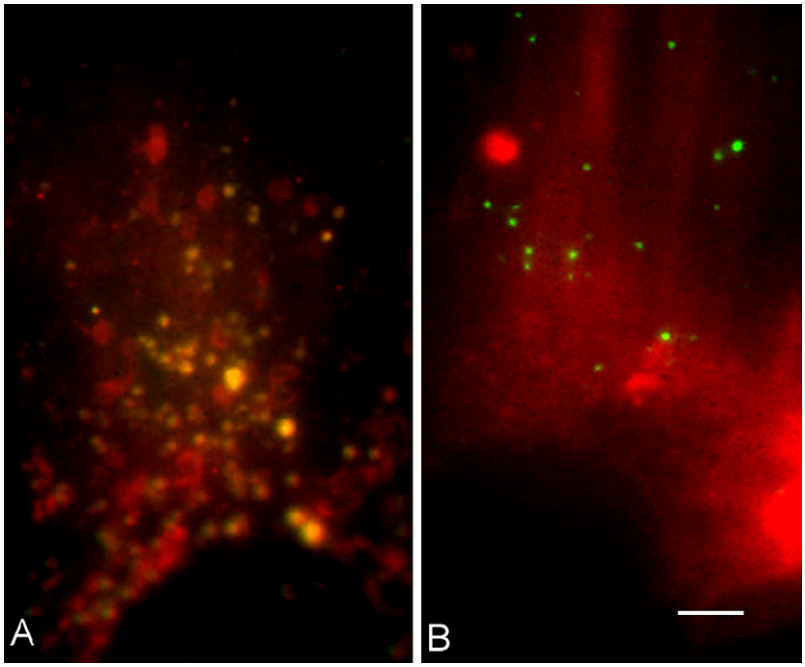

FIGURE 1 Osmotic lysis of pinosomes. (*A*) Under hypertonic loading conditions, pinosomes in COS-7 cells are labeled with FITC-dextran (*red*) and are visible near the plasma membrane by TIRF microscopy. At this stage, Qdot:myoVa HMM complexes (*green*) localize to pinosomes, producing the yellow colocalization signal. (*B*) After lysis of pinosomes by hypotonic shock, FITC-dextran forms a uniform haze throughout the cytosol of the cell, whereas Qdot:myoVa conjugates are free and motile within the cell. Scale bar: 5 μm.

MATERIALS AND METHODS

Protein constructs and Qdot conjugation

A mouse myoVa construct, truncated after amino acid 1098 to produce a double-headed HMM fragment, was tagged at either the N- or C-terminus with an 88-amino acid biotin ligase recognition sequence (7,16). Using a Baculovirus/Sf9 cell system, the myosin heavy chain was coexpressed with calmodulin light chains that were mutated to be calcium-insensitive (CaM Δ-all), eliminating the inhibitory effects on myoVa processivity that accompanies light chain dissociation (17). A C-terminal FLAG tag on the myosin heavy chain facilitated protein purification by affinity chromatography (17). A single-headed myoVa subfragment-1 (S1) construct was generated by truncation after amino acid 908, which was tagged at the C-terminus with a biotin ligase recognition sequence and expressed and purified as above.

Purified myoVa was conjugated to either 565 nm or 655 nm emitting streptavidin-coated Qdots (Invitrogen, Carlsbad, CA) in buffer A (25 mM imidazole, pH 7.4, 0.3 M KCl, 4 mM $MgCl_2$, 1 mM EGTA, 10 mM DTT, and 0.1 mg/mL BSA). To ensure that a Qdot was conjugated to a single motor, Qdots and N-terminal biotin myoVa were mixed at a 5:1 molar ratio (i.e., 30 μM Qdots to 6 μM myoVa) in buffer A for 10 min at room temperature (25°C). Under these conditions and assuming Poisson statistics, 91% of the Qdots would have no more than one attached motor, and thus the Qdot would be attached to only one of the two heads. For experiments focusing on Qdot transport by multiple motors, the mixing ratio was 1:4 with 30 μM Qdots and 120 μM C-terminal biotin-myoVa. This ratio would produce a mixture with 94% of the Qdots having three or more attached motors, with binding to the Qdot saturating at four motors based on previous studies (16).

To confirm that the observed Qdot transport in COS-7 cells resulted from active myoVa motors, control experiments were performed in which Qdots were conjugated to either bovine serum albumin (BSA) or chemically modified myoVa. The BSA-coated Qdots were formed by conjugating 30 μM streptavidin-Qdots with 150μM biotinylated-BSA (Pierce Biochemical, Rockford, IL) in buffer A for 10 min at room temperature. Sulfhydryl modification of expressed myoVa HMM, using *N*-ethylmaleimide (NEM), resulted in a nonfunctional myoVa that no longer bound actin. NEM stocks were prepared at 3.75% (w/v) in ethanol and then added to HMM MyoVa (final concentration 0.1 mg/mL) in 500 μM EGTA, 500 μM sodium azide, 6.25 mM imidazole. The reaction was allowed to proceed for 5–45 min at room temperature and then stopped by the addition of 1 M DTT. The lack of actin binding and the processive movement of NEM-treated myoVa constructs were determined in the in vitro single-molecule TIRF assay (4,5).

Cell culture studies

COS-7 cells were grown in Dulbecco's modified Eagle's medium (DMEM) enriched with 10% (v/v) FBS, with 5% CO_2 at 37°C on 35 mm petri dishes with No. 1 coverglass bottoms (MatTek, Ashland, MA). These cells are extremely flat and tightly adherent to the coverglass, which makes them good candidates for TIRF microscopy.

Qdot:MyoVa conjugates were delivered into cells by osmotic lysis of pinosomes (18,19). Briefly, cells were incubated in hypertonic loading medium (DMEM with 0.5 M sucrose and 10% w/v poly-ethylene glycol 1000) along with 7.5 nM Qdot:MyoVa conjugates for 10 min at 37°C. The cells were then shocked in hypotonic lysis medium (DMEM and water in a 3:2 ratio) for 2 min at room temperature. The cells were then returned to DMEM and imaged at room temperature as described below.

To witness the incorporation of Qdot:myoVa conjugates into pinosomes and their subsequent release into the cytoplasm, pinosomes were labeled by the addition of 5 mg/mL FITC-Dextran 500K (Sigma, St. Louis, MO) to the hypertonic loading medium during the delivery of Qdot:myoVa conjugates (see above). After a 10 min incubation at 37°C, the cells were then washed three times with hypertonic loading medium and imaged for pinosome encapsulation of the Qdot:myoVa conjugates (Fig. 1 *A*). To confirm that the Qdot:-myoVa conjugates were released into the cytoplasm upon pinosome lysis, the cells were then osmotically shocked (see above) and imaged (Fig. 1 *B*).

To demonstrate that Qdot:myoVa movement was an ATP-dependent process, intracellular ATP was reduced by inhibiting its synthesis. Cells were incubated at 37°C for up to 30 min in glucose-free MEM with 0.05% sodium azide, an oxidative phosphorylation inhibitor, and 10 mM 2-deoxy-D-glucose, an anaerobic glycolysis inhibitor (all obtained from Sigma Aldrich). During this treatment, the cells underwent apoptosis as the intracellular [ATP] fell. Therefore, Qdot:myoVa motion was characterized within a 30 min treatment period, given that longer treatments resulted in significant changes in overall cell morphology and eventual release from the coverglass surface.

Image acquisition and data analysis

Cell culture plates were transferred to a Nikon TE2000 inverted microscope equipped with a PlanApo objective lens (100×, 1.49 n.a.) for through-the-objective TIRF microscopy. Qdots were excited at 488 nm with an argon laser. Images were obtained at 60 frames/s with 2 × 2 pixel binning (58.5 nm pixel resolution) using an intensified CCD camera (XR Mega-S30 running Piper Control v2.3.14 software; Stanford Photonics, Stanford, CA). Dual-color, simultaneous imaging was achieved with the use of a dual-view beam splitter (Optical Insights, Pleasanton, CA). Typically, 1000 images were recorded for each stack and 20 stacks were recorded per dish of cells.

Image analysis was performed using ImageJ 1.37v (National Institutes of Health, Bethesda, MD). Qdots were tracked in the x,y visual plane using SpotTracker 2D (20) to generate motion paths in two dimensions. The spatial resolution of the imaging system was determined by tracking a stationary Qdot within a cell over 1000 frames. The 15 nm standard deviation (SD) position error of this Qdot in both the x and y axes reflects the system's spatial resolution. Qdot:myoVa conjugate velocities were determined from the slope of a displacement versus time plot for straight line motion paths that persisted for more than 20 frames.

The MSD over multiple time intervals is calculated as:

$$\mathrm{MSD}(n\Delta t) = \frac{1}{N-n}\sum_{i=1}^{N-n}\left[(x_{i+n}-x_i)^2+(y_{i+n}-y_i)^2\right], \tag{1}$$

where N is the total number of frames in the trajectory, n is the number of frames for different time intervals over which the MSD is being calculated, Δt is the time (16.6 ms) between frames, and x_i and y_i are the positions of the Qdot in frame i (21). Diffusion coefficients are calculated as one-fourth of the slope of the MSD versus the time interval relationship when plotted on linear axes.

For various modes of motion, the relationship between the MSD and the time interval ($n\Delta t$) can be generalized by MSD ~ $(n\Delta t)^{\alpha}$ (22), where α is the "diffusive exponent". For an immobile particle, $\alpha = 0$, as displacement does not change with time. For a randomly moving particle $\alpha = 1$, and for a particle moving in a straight line at a constant velocity $\alpha = 2$. For this study, the diffusive exponent (α) was determined from the slope of the relationship between the MSD and time interval ($n\Delta t$) on log-log axes. The MSD was calculated using internal averaging, which is also known as "averaging over all pairs", as this allowed use of the full data set with equal weighting for each data point (22). For this study, trajectories were composed of 1000 frames each, and MSD analysis was limited to $n \leq 120$ or a time interval of 2.0 s. The short timescale behavior of trajectories, termed $\alpha_{(0\text{–}0.2\ s)}$, is characterized by linear fits to the first 12 data points (i.e., up to 0.2 s) of individual MSD plots on log-log axes.

To compare $\alpha_{(0\text{–}0.2\ s)}$ values under different experimental conditions, cumulative probability distributions were plotted. Such an analysis is independent of bin width. Cumulative probability distributions were generated by calculating the probability (i.e., the proportion of the total number of points in the data set) that any data point would be $\leq x$. Fits applied to the cumulative probability distributions were based on the mean and SD of the data, assuming a normal (Gaussian) distribution. Because the populations are well fit as Gaussian distributions, they were compared using Welch's two-sample t-test.

Given myoVa's inherent stepping rate, the imaging rate of 60 frames/s was sufficient to detect steps generated by a single myoVa motor. These steps were identified in displacement versus time traces by an unbiased, statistically based MATLAB software (The MathWorks, Natick, MA) routine (23). The step dwell time histograms were fit by $F(t) = tk^2e^{-kt}$ rather than a single exponential. Since the stepping data were consistent with only one of the two myoVa heads being Qdot-labeled at its N-terminus, for each observed step there was an unobserved "silent step" from the unlabeled head, which occurred at the same rate (6).

The same Qdot:myoVa conjugates delivered intracellularly were characterized for their in vitro run lengths and velocities on single actin filaments in the single-molecule TIRF assay as described previously (5). However, the ionic strength of the in vitro assay buffers was increased with 200 mM KCl to approximate the intracellular ionic strength and to allow more meaningful comparisons to be made between the in vitro Qdot:myoVa velocities and that measured intracellularly. These in vitro ionic conditions were used for both the single motor and many motors per Qdot regime. Mean velocities were compared using Welch's two-sample t-test, and their variances were compared using the F-test.

RESULTS

Qdot-labeled MyoVa delivery into cells

Qdot:myoVa conjugates were delivered into COS-7 cells by osmotic lysis of pinosomes (18,19). This delivery protocol proved to be quick and effective, and allowed for the treatment of an entire plate of cells (10^5 cells) in <15 min. Although intracellular delivery by lipofection was considered, the Qdot:myoVa conjugates were effectively trapped within intracellular vesicles. After lipofection was completed per the manufacturer's protocol (Lipofectamine 2000; Invitrogen, Carlsbad, Ca), the Qdots were colocalized for up to 2 h posttreatment to membrane-bound vesicles, which were identified using a lipophilic dye (Vybrant DiI; Invitrogen, Carlsbad, CA). The resulting data (not shown) suggest that the Qdot:myoVa conjugates remain internalized within a vesicular compartment, and that motion of the Qdot:myoVa conjugates could result from endogenous motors transporting the encapsulated Qdot cargo.

To test whether a similar situation would occur with pinocytosis, FITC-dextran and Qdot:myoVa conjugates were simultaneously added to the hypertonic loading medium. As pinosomes formed, both FITC-dextran and Qdot-myoVa were colocalized within these vesicles (Fig. 1 *A*). The pinosomes were then lysed by hypotonic shock and released their contents, after which a diffuse FITC-dextran haze was observed throughout the cytosol and numerous Qdot:myoVa conjugates underwent significant motion (Fig. 1 *B*; see Movie S1 in the Supporting Material). During image acquisitions up to 200 s, the Qdot:myoVa conjugates remained within the ~150 nm thick evanescent TIRF field, suggesting that these conjugates were restricted to the actin cortex.

The following controls confirmed that Qdots observed in the TIRF field were conjugated to active myoVa. When bare Qdots, BSA-conjugated Qdots, or Qdots conjugated to a nonfunctional, NEM-modified myoVa motor were delivered into cells, Qdots were infrequently observed in the TIRF field, but were readily visualized beyond the evanescent field using far-field illumination (Fig. S1 *D*, *inset*). This observation was confirmed more dramatically by simultaneously delivering equal amounts of two different-colored Qdot conjugates (i.e., 565 nm and 655 nm emissions): one conjugated with BSA and one conjugated with myoVa HMM. After pinocytosis was completed, the motor-conjugated Qdots outnumbered BSA-conjugated Qdots within the TIRF field by more than 600 to one (Fig. S1, *A* and *B*). A similar result was obtained when the Qdot colors were reversed (Fig. S1, *C* and *D*).

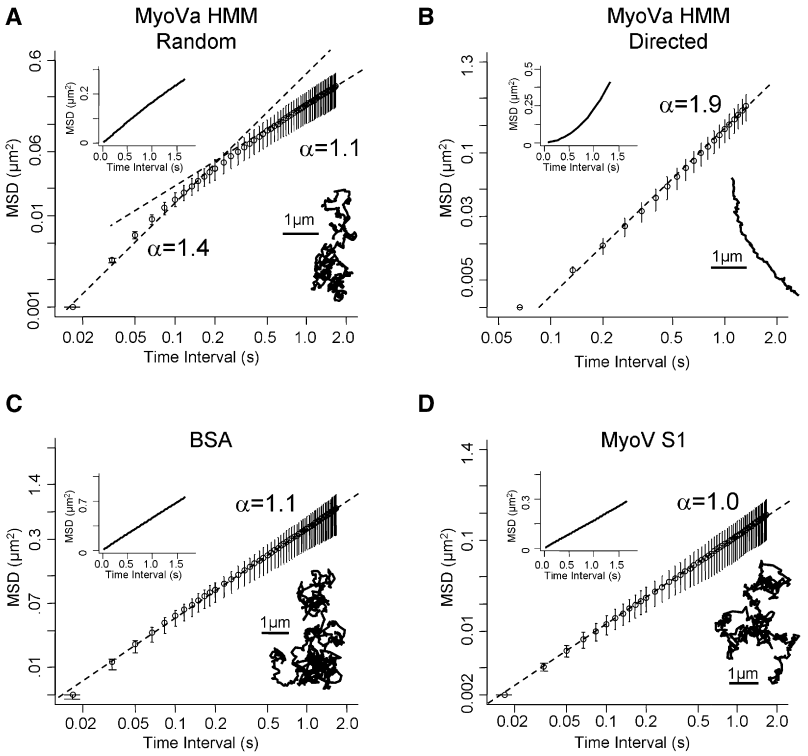

FIGURE 2 Modes of motion of various Qdot-labeled proteins. Example trajectories and ensemble MSD plots are shown on both linear axes (*inset graphs*) and log-log axes (*large graphs*). The trajectories and their corresponding MSD plots are shown for Qdot:myoVa HMM conjugates undergoing random (*A*) and directed (*B*) motion, as well as data from Qdot:BSA (*C*) and Qdot:myoVa S1 (*D*) conjugates. The MSD plots are those of ensemble-averaged MSD traces for each of the conjugates. The directed Qdot:myoVa HMM MSD ($n = 5$) has an $\alpha = 1.9$ (*dashed line*) indicative of an active process. The Qdot:myoVa HMM MSD for random trajectories ($n = 120$) displays hyperdiffusive behavior at short time intervals ($\alpha_{(0\text{-}0.2\ s)} = 1.4$, *dashed line*), which is unique to intact, processive myoVa HMM, whereas Qdot:BSA ($n = 31$) and Qdot:myoVa S1 fragments ($n = 61$) show random motion at all timescales, consistent with diffusion, as described by $\alpha = 1.0$ (indicated by the *dashed lines*).

Single-particle analysis of Qdot:myoVa motion

Visual inspection of the Qdot:myoVa movements indicated that most of the trajectories (96%, $n = 125$) appeared random in nature (Fig. 2 *A*, Movie S2), although a few trajectories were clearly directed for greater than a micron (Fig. 2 *B*, Movie S3). As a control for a particle undergoing purely diffusive movements, Qdot:BSA conjugates were also delivered into cells (Fig. 2 *C*, Movie S4). To characterize these movements, individual trajectories were subjected to MSD analysis. When plotted on linear axes, a parabolic MSD relationship is indicative of a directed process, such as motor-driven transport (as in Fig. 2 *B*, *inset*). MSD plots originating from random motion, such as a diffusive process, are linear (Fig. 2 *C*, *inset*), and in this case they yielded a diffusion coefficient of $0.15 \pm 0.12\ \mu m^2 s^{-1}$. The MSD relationships for most of the myoV trajectories plotted on linear axes (Fig. 2 *A*, *inset*) were similar to those of the Qdot:BSA conjugates, giving an effective diffusion coefficient of $0.21 \pm 0.05\ \mu m^2 s^{-1}$.

With similar trajectories, MSD plots, and diffusion coefficients for the BSA and the majority of myoVa conjugates, one might conclude that the myoVa trajectories are not motor-driven, but rather are diffusive in nature. The existence of directed trajectories that are presumably myoVa-dependent (Fig. 2 *B*), however, suggests that some component of the random trajectories may involve myoVa transport. Therefore, we analyzed the random myoVa trajectories in greater detail, focusing on timescales that might correspond to the duration of short myoVa run lengths (i.e., ~0.35 s for a 200 nm run length, assuming an in vitro velocity of 580 nm/s; see Table 1). To emphasize these short timescales, MSD relationships for the various conjugates were generated for each conjugate from an ensemble of trajectories and then plotted on log-log axes (large MSD plots in Fig. 2).

When plotted on log-log axes, the MSD slope defines the diffusive exponent (α; see Materials and Methods), with $\alpha = 1$ indicating random motion (21), as observed for the Qdot:BSA conjugates (Fig. 2 *C*; $\alpha = 1.1 \pm 0.1$, $n = 31$), and $\alpha = 2$ resulting from a directed process, as with the Qdot:myoVa conjugate trajectories that were clearly directed (Fig. 2 *B*; $\alpha = 1.9 \pm 0.3$, $n = 5$) over all timescales. Of interest, the MSDs for the apparently random Qdot:myoVa trajectories are biphasic (Fig. 2 *A*). An $\alpha_{(0\text{-}0.2\ s)} = 1.4 \pm 0.2$ ($n = 120$) was obtained for short timescales by plotting cumulative probability distributions of α for the first 0.2 s from individual MSD plots (Fig. 3), which is significantly

TABLE 1 Summary of intracellular and in vitro velocities

	One motor		Many motors		*p*-Value
	Velocity +/− SE (nm/s)	*n*	Velocity +/− SE (nm/s)	*n*	
Intracellular	604 ± 36	44	591 ± 40	42	0.959
In vitro	580 ± 23	67	604 ± 26	59	0.246
p-Value	0.279		0.747		

In vitro data were obtained with 200 mM KCl buffer to approximate the intracellular ionic strength. Statistical comparisons were made using the Kolmogorov-Smirnov, which does not assume a parametric distribution of the data and is independent of bin width (25).

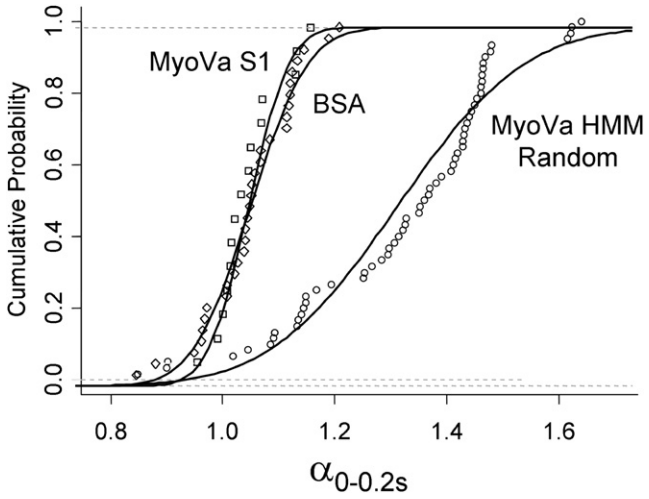

FIGURE 3 Cumulative probability distributions of $\alpha_{(0\text{-}0.2\ s)}$. At short timescales ($\leq$0.2 s) the initial slope, $\alpha_{(0\text{-}0.2\ s)}$, of the MSD on log-log axes was determined for all trajectories associated with the Qdot:myoVa HMM, Qdot:myoVa S1, and Qdot:BSA conjugates. The Qdot:myoVa HMM shows hyperdiffusive behavior, with an $\alpha_{(0\text{-}0.2\ s)}$ shifted to higher values compared to either the BSA or S1 conjugates, which are close to 1.0 as expected for a diffusive process.

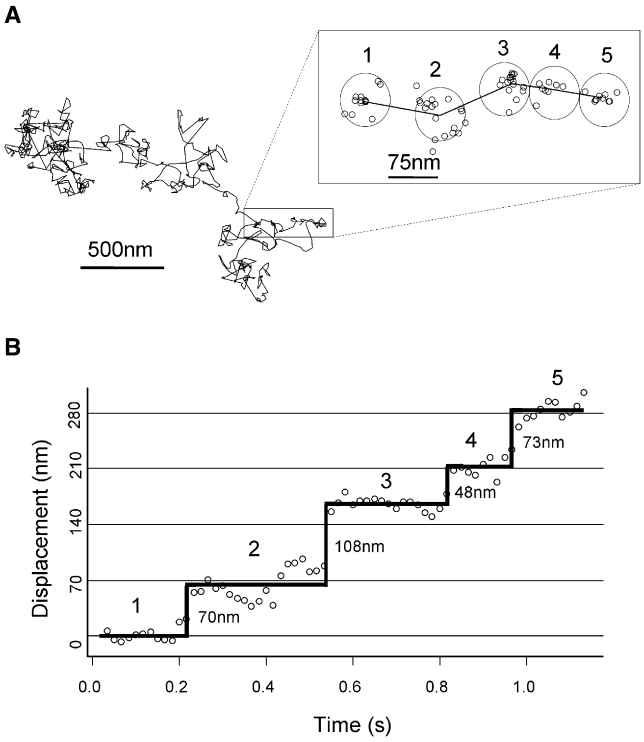

FIGURE 4 High spatial and temporal resolution tracking of Qdot:myoVa HMM trajectories in cells. (*A*) An example *x*, *y* position trajectory imaged at 60 frames/s for a total elapsed time of 16.7 s; the inset is an expanded view of the indicated trajectory segment with individual steps highlighted by circles. (*B*) Displacement versus time representation of the same trajectory segment shown in the inset in *A*, with the individual steps numbered as in the inset. Steps are fit as described in Materials and Methods.

greater ($p < 0.001$) than the $\alpha = 1.1 \pm 0.2$ ($n = 120$) for timescales $\geq$ 1.0 s. This biphasic MSD suggests that these random trajectories are not consistent with passive diffusion; rather, they are hyperdiffusive and presumably the result of the attached myoVa motor at short timescales.

Does the apparently directed component in the otherwise random myoVa trajectories arise from myoVa's association with some other endogenous motor or process? As a control, single-headed myoVa S1 fragments conjugated to Qdots were introduced into cells and then tracked and analyzed (Fig. 2 *D*, Movie S5). The S1 fragments are biochemically active but are incapable of processive movement, which requires a double-headed motor. As expected, the Qdot:myoVa S1 conjugates displayed random-appearing trajectories (Fig. 2 *D*) very similar to those of the Qdot:BSA conjugates (Fig. 2 *C*). These were characterized by linear MSD plots with an $\alpha = 1.0 \pm 0.2$ ($n = 61$; Fig. 2 *D*), which is no different from the Qdot:BSA conjugates ($p > 0.87$), consistent with pure diffusive movement, and by a diffusion coefficient of $0.06 \pm 0.04\ \mu m^2 s^{-1}$. The lower diffusion coefficient compared with the Qdot:BSA conjugates may reflect the transient trapping of the Qdot within the actin cortex by the attached S1 molecules.

MyoVa stepping and velocities

As a more stringent test to determine whether the observed Qdot motion was generated by a processive myoVa molecule, we observed the motor's individual steps within random trajectories by conjugating the streptavidin-Qdot to the biotinylated N-terminus of the motor domain (7). Using the MSD results to guide our subsequent analysis of the random Qdot:myoVa trajectories, we identified linear segments that persisted $\leq$1.0 s (Fig. 4 *A*) and analyzed the individual steps at high time (16.6 ms) and spatial (15 nm) resolution (Fig. 4 *B*). Using an unbiased statistical algorithm to identify steps within a noisy displacement versus time trace (see Materials and Methods), we detected individual 75 $\pm$ 2 nm ($n = 127$) steps in short segments that were associated with 24 separate trajectories (Fig. 5, *A* and *B*) and arose from the population of myoVa molecules that were Qdot-labeled on only one head (7). Although it is possible that some of the molecules have both heads that were Qdot-labeled, the 36 nm spatial separation between heads while the motor paused (7) prevented us from discerning the motion of either head, due to the 15 nm spatial resolution. Occasional backsteps were also observed (Fig. 5 *A*), as reported recently for a single myoVa stepping against low resistive loads in the optical trap (24). The dwell time histogram for the observed steps (see Materials and Methods for analysis) resulted in a mean stepping rate of 16 $\pm$ 1 s^{-1} (Fig. 5 *C*).

The mean velocity associated with linear segments as described above was 604 $\pm$ 36 nm/s. This velocity is not significantly different from that observed for the same construct in the in vitro single-molecule TIRF assay (Table 1). The intracellular velocity distribution exhibited a 2.7-fold greater variance ($p < 0.0005$), which may reflect the more

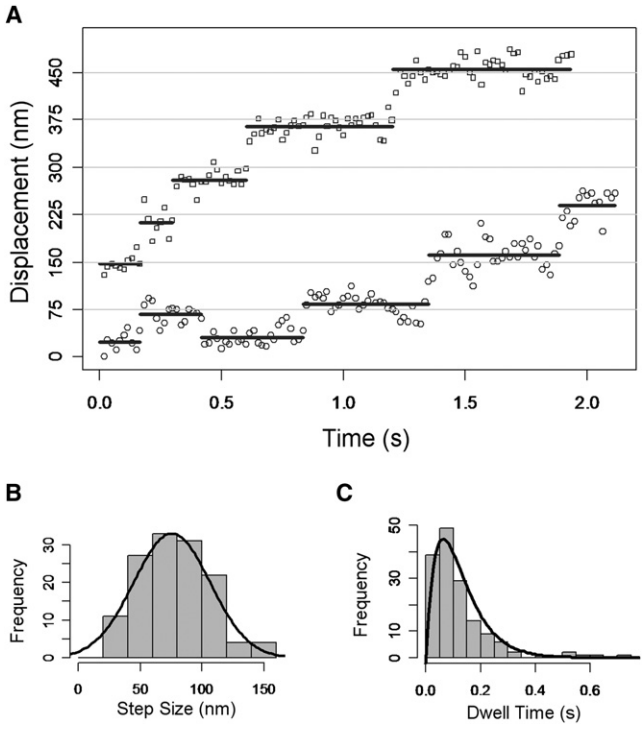

FIGURE 5 Intracellular stepping of MyoVa. (*A*) Two displacement versus time traces from Qdot:myoVa HMM conjugates derived from trajectories that are random in appearance (see Figs. 2 *A* and 4 *A*) with steps identified by the step finding algorithm (see Materials and Methods). A backstep is apparent in the lower trace. (*B*) A step size histogram (75 ± 2 nm (mean ± SE), $n = 127$) for steps derived from linear segments of random-appearing trajectories. (*C*) The dwell time histogram was fit to $F(t) = tk^2e^{-kt}$ (see Materials and Methods) to derive a stepping rate of $k = 16 \pm 3\ s^{-1}$.

complex and dynamic nature of the cellular environment. To confirm that these short runs resulted from an ATP-dependent process, intracellular ATP levels were effectively reduced by metabolic inhibition (see Materials and Methods). After this treatment, the mean intracellular Qdot:myoVa velocity was reduced 50% (314 ± 33 nm/s, $n = 20$), further supporting the idea that the random Qdot:myoVa trajectories have an active, ATP-dependent component.

Although we observed a single myoVa stepping processively, as described above, intracellular cargo transport may involve multiple motors sharing this responsibility (14). To mimic multiple-motor transport, we used a myoVa HMM construct that was biotinylated at the C-terminus, which allowed the attachment of up to four motors (16) to a single streptavidin-conjugated Qdot (see Materials and Methods). The in vitro run lengths for these Qdot-myoVa conjugates (1321 ± 116 nm, $n = 59$) were nearly twice as long as that for a single motor (801 ± 56 nm, $n = 67$), confirming that multiple motors were attached to the Qdot (Table 1). When these multiple-motor Qdot conjugates were delivered into cells, the intracellular velocities were the same as that exhibited by a single motor, as was the case in vitro (Table 1).

DISCUSSION

MyoVa's processive stepping and its ability to maneuver through actin filament intersections in vitro (4) may contribute to this unconventional myosin's capacity to transport intracellular cargo. MyoVa's role in normal cellular function is highlighted by human myoVa gene mutations that lead to Griscelli syndrome, a disorder characterized by albinism and either neurological impairment or immunodeficiency (26,27). Although its ability to transport cargo as it steps processively has been characterized extensively in vitro, direct evidence of this within cells is lacking. To address this, we introduced Qdot-labeled myoVa into mammalian COS-7 cells by pinocytosis and characterized the intracellular motion paths associated with single myoVa motors using TIRF microscopy, with imaging limited to the subplasmalemmal actin cortex. Using this approach, we observed the individual steps of a single myoVa HMM motor as it processively carried its Qdot cargo through the actin cytoskeleton. In addition, the velocity of cargo transport was independent of the number of attached myoVa motors regardless of whether transport was characterized in vitro on single actin filaments or within the complex intracellular environment.

Characteristics of intracellular MyoVa motion

The enrichment of Qdot:myoVa HMM conjugates within the TIRF field of illumination (see Results) after their release from pinosomes suggests that the actin cortex may act as a spatial filter to confine active Qdot:myoVa HMM conjugates. Of interest, the majority of motion paths associated with these conjugates were random in appearance (Fig. 2 *A*), with only an occasional directed trajectory (Fig. 2 *B*). Given that the cortical actin meshwork is composed of numerous actin filament intersections and Arp2/3 junctions (28), the random trajectories may arise from a myoVa motor taking a ''random'' walk along this complex actin network. This is supported, as discussed below, by 1), a detailed characterization of trajectories through MSD analysis; 2), the detection of individual myoVa steps within segments of random trajectories; 3), the decreased velocity of Qdot:myoVa HMM motion at lowered ATP concentration; and 4), Monte Carlo simulations of myoVa processive transport along a defined actin filament network.

MSD analysis

MSD analysis provides a means of distinguishing between particle motions that are thermally driven and those that are driven by directed movements generated by a molecular motor. When plotted on log-log axes, the MSD slope (α) is characteristically 1.0 for random motion and 2.0 for directed transport (21). The MSD plots of Qdot:myoVa HMM conjugates had a significantly ($p < 0.001$) steeper slope ($\alpha = 1.4$) at short timescales (i.e., $\leq$0.2 s; Figs. 2 and 3), but were

comparable to BSA or S1 at longer timescales ($\alpha = 1.1$; Fig. 2). Thus, the random Qdot:myoVa HMM trajectories cannot be described as purely diffusive; rather, they must have a directed component contributing to motion at short timescales. In further support of this, Qdot:myoVa S1 conjugates, which show no appreciable actin-binding or processive behavior in vitro (see Results), exhibit MSD with an α similar to that of the diffusive Qdot:BSA conjugate (Figs. 2, *C* and *D*, and 3). Of interest, a similar crossover in MSD plots, going from enhanced ($\alpha = 1.5$) to thermally based random motion ($\alpha = 1$), was reported for microsphere trajectories in SV80 cells (29). The authors concluded that the enhanced diffusion could be attributed to microtubular-based motor transport in the perinuclear microtubule meshwork, since microsphere trajectories become purely diffusive after treatment with nocodazole to depolymerize microtubules.

MyoVa intracellular stepping and velocities

One trivial explanation for the directed component in the Qdot:myoVa HMM MSD is that the complex associates with an endogenous myosin motor and becomes its cargo. If so, Qdot displacements would reflect the stepping behavior of the endogenous motor. However, the large sequential 75 nm steps observed in short segments of the random Qdot:myoVa HMM trajectories (Figs. 4 and 5) are only consistent with a processively stepping myoVa molecule labeled on one head (7). If the labeled myoVa were the cargo of an endogenous myosin, steps of half that size (~37 nm) would be expected, reflecting displacement of the endogenous motor's center of mass.

The observed 16 s^{-1} stepping rate is similar to the ADP-release rate that is rate limiting for ATP hydrolysis and processive stepping in vitro (12,30,31). Thus, the average velocity for this stepping behavior is 600 nm/s, assuming that the motor's center of mass is displaced by half the distance traveled by each of its heads (i.e., 37.5 nm). This velocity is similar to the mean velocity (604 $\pm$ 36 nm/s) measured for short, straight-line segments within random trajectories where individual steps were not easily detected. The intracellular velocities are in excellent agreement with the in vitro velocity determined for these same Qdot:myoVa conjugates under conditions mimicking intracellular ionic strength (Table 1). The reduction in intracellular velocities observed after metabolic poisoning to lower the cellular ATP content is also consistent with active stepping by myosin.

If Qdot:myoVa conjugates were prone to perpendicular motion relative to the optical plane, it would have been impossible to observe individual motors for up to 200 s within the ~150 nm TIRF field of illumination. Additionally, the two-dimensional (2D) motion projections visualized here would tend to underestimate both the motor's velocity and step size. Since these measurements were identical for the in vitro (7) and intracellular environments, we feel confident that the the 2D particle tracking is valid because the actin cortex effectively becomes 2D as it lies parallel to the cell surface in contact with the coverslip.

Taken together, these data provide strong evidence that the observed Qdot motion (at least for portions of the random trajectories) is due to a single myoVa molecule stepping along actin tracks within the cell cortex.

Monte Carlo simulations of MyoVa motion trajectories

To understand the extent to which myoVa contributes to the observed motion, we developed a simple model (see the Supporting Material for details) to simulate four potential scenarios of Qdot:myoVa motion constrained to the visual plane, in which the motor 1), steps processively along a single actin filament; 2), steps processively along an actin network containing intersections; 3), steps processively along an actin network 50% of the time and freely diffuses the other 50%; or 4), only undergoes pure diffusion.

The basic assumptions in this model are that 1), the Qdot is transported by a single processive myoVa HMM with experimentally determined step size and dwell time distributions (12,24,30,31); 2), when confronted with an actin-actin intersection, the probability that the motor turns or continues through the intersection is defined by previous in vitro studies (4); 3), the randomly oriented actin filament meshwork (Fig. 6 *B*) is defined by a characteristic distance (i.e., 125 nm) between actin-actin intersections based on EM images of the cortical actin cytoskeleton (28,32); and 4), the time and spatial resolutions for the Qdot position are defined by the experimental system used in this study. With these simple assumptions, 1000 simulated trajectories for the four hypothetical cases described above were generated and an ensemble-averaged MSD was calculated and plotted on log-log axes (Fig. 6 *C*). In addition, the MSD slope for short timescales (up to 0.2 s; $\alpha_{0\text{-}0.2\ s}$) was fit and a cumulative probability plot was generated (Fig. 6 *D*).

Fig. 6 *A* shows a portion of a displacement versus time trace from a simulated trajectory for a myoVa moving processively along a straight actin filament (case 1), as seen in the single-molecule in vitro TIRF assay (4,5). The ensemble-averaged MSD plot was described by an $\alpha = 1.8 \pm 0.03$ over all timescales (Fig. 6, *C* and *D*), close to the expected value of 2 for a directed process. The slightly lower α for the simulation is largely due to the dwell time of the motor as it steps along the actin filament. On closer inspection, the motor's stepping behavior, even under ideal conditions, can be described as periods of constrained motion (i.e., during its dwell time) interspersed with sudden 75 nm steps. By MSD analysis, constrained motion is described by an $\alpha < 1$. Thus, the existence of apparent constrained motion as the motor pauses between steps results in a depressed MSD slope, particularly at the shortest timescales. MSD values are also depressed by the modeled uncertainty of the myoVa position based on the spatial resolution of the

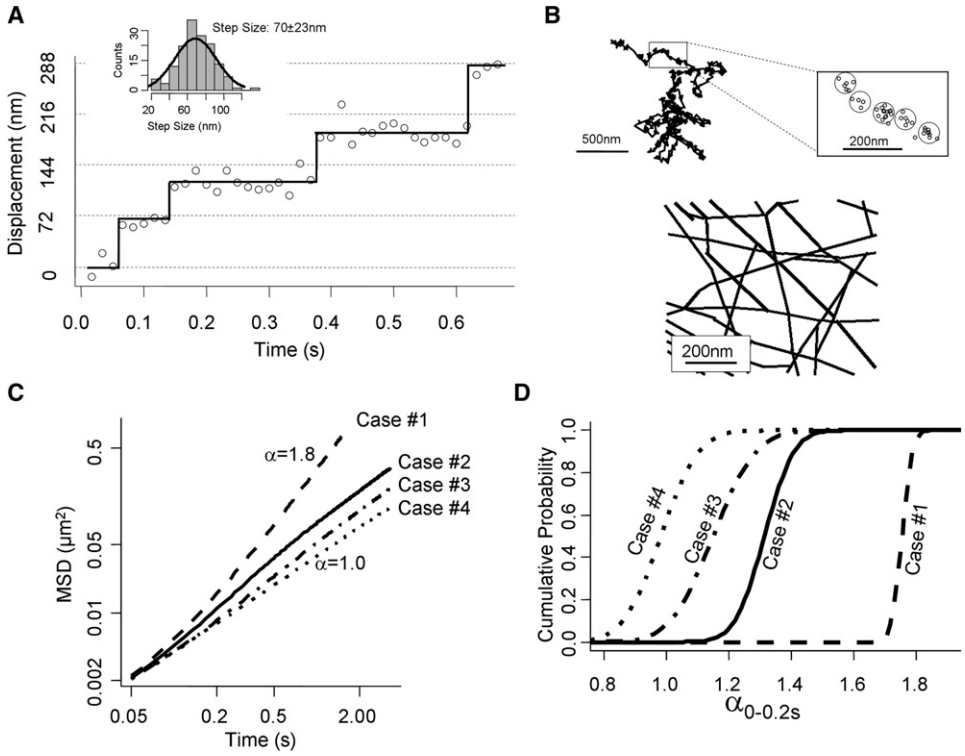

FIGURE 6 Monte Carlo simulation of MyoVa modes of motion. (For details of the model simulations, see Discussion and Supporting Material.) (*A*) Simulation of myoVa processively stepping on single, straight actin filament, as seen in single-molecule TIRF assays. The step detection algorithm recovers a mean step size of 70 ± 23 nm ($n = 139$) similar to the 72 nm step size used in generating the trajectories. (*B*) Simulated myoVa HMM trajectory of a processive random walk through a complex actin filament network (see filament tracing) is described by a highly convoluted trajectory. Individual steps are apparent during trajectory segments and are similar to experimental results. A tracing of the cortical actin network taken from Svitkina et al. (28) is used to define the distance between actin-actin intersections. (*C*) Ensemble MSD analysis on log-log axes of 1000 simulations as in *B* (case 2, *solid line*) reveals a relationship with an initial slope of 1.3, which falls to 1.0 at longer timescales. MSD for simulations of a purely diffusive Qdot:myoVa (case 4, *dotted line*) has a slope, α, of 1.0 at all timescales, as expected for a diffusive process. For processive trajectories on a single straight actin filament, the MSD simulation results in $\alpha = 1.8$ at all timescales (case 1, *dashed line*). (*D*) Cumulative probability distribution of $\alpha_{(0\text{-}0.2\ s)}$ for trajectory simulations: case 1, processive movement of straight actin filament; case 2, processive movement on actin filament network as in *B*; case 3, processive movement on actin network 50% of the time and purely diffusive for the remaining 50%; case 4, purely diffusive.

optical system (see Fig. S4). At the opposite extreme (case 4), the simulated trajectories for a purely diffusive Qdot:BSA conjugate (trajectory not shown) give a linear MSD plot over all timescales (Fig. 6 *C*) but with an $\alpha_{0\text{-}0.2\ s} = 1.0 \pm 0.1$, as expected for a diffusional process (Fig. 6 *D*). For case 2, in which the motor steps processively on a randomly oriented actin filament network, the simulated trajectory is extremely convoluted, arising from myoVa's propensity to turn at an intersection (Fig. 6 *B*). These trajectories are similar to those observed experimentally, having short segments with detectable 75 nm steps. In fact, the ensemble-averaged MSD plot (Fig. 6, *C* and *D*) shows a biphasic nature similar to that of the plot observed experimentally, with a simulated $\alpha_{0\text{-}0.2\ s} = 1.3 \pm 0.1$ at short timescales and 1.0 ± 0.3 at longer timescales. Case 2 alone provides significant insight to the interpretations of an MSD relationship. In this case, we assume that the myoVa never leaves the actin tracks and thus diffusional processes do not contribute to the trajectory. Without prior knowledge, the resultant trajectory and MSD could have been interpreted as having a significant diffusive component given its $\alpha = 1$ at longer timescales. Finally, for case 3, in which the motor spends half of its lifetime processively stepping while the other half is in pure diffusion, the $\alpha_{0\text{-}0.2\ s} = 1.2 \pm 0.1$ at short timescales, falling to 1.0 at longer timescales (Fig. 6 *D*).

Two important insights were derived from this modeling effort: 1), at long timescales, MSD analysis cannot distinguish between a Qdot-labeled motor undergoing pure diffusion or one that is processively stepping along a randomly oriented actin filament network; and 2), at short timescales (~0.2 s), the reduction in α from the expected value of 2 for a processive motor is dependent on the distance between actin-actin intersections, the probability that the motor will turn at an intersection, and the proportion of the motor's lifetime that will be spent undergoing diffusion (see Supporting Material). Thus, in light of the model, the experimentally obtained $\alpha_{0\text{-}0.2\ s} = 1.4 \pm 0.2$, with its lower estimate of $\alpha_{0\text{-}0.2\ s} = 1.2$ (i.e., 1 SD), suggests that the myoVa motor spends at least half of its lifetime taking a processive random walk along the actin cytoskeleton.

In vitro versus cellular velocities

Intracellular cargo transported by myoVa, such as melanosomes, may have as many as 60 attached motors (14). If multiple motors on the cargo surface can simultaneously interact with the actin track, the transport velocity could vary with the number of engaged motors. Kural and coworkers (8) proposed that the unusually high velocities for peroxisome transport by kinesin in cells compared with in vitro estimates for a single kinesin motor may result from multiple motors sharing the workload. More recently, Yoo and co-workers (33) delivered Qdot:kinesin conjugates into cells via a lipid-based internalization protocol, and also

reported higher velocities for these motors compared with in vitro measurements. The fact that both groups reported higher intracellular velocities for kinesin transport suggests that movements of the microtubular track, whether thermally based or derived by interactions of other motors with the cytoskeletal track, may have contributed to the high speeds of cargo movement (34–36).

Here we took advantage of our Qdot-labeling strategy to compare single and multiple myosin motor transport in vitro and within cells. The velocities for single and multiple myoVa motor transport were the same for both in vitro and inside cells (Table 1). This result suggests that the intracellular environment may not pose a physical barrier to cargo transport (37), at least for cargo with dimensions comparable to the ~20 nm diameter Qdot. Similarly, there is no evidence that cargo velocity powered by multiple kinesin motors within cells is enhanced above the capacity inherent to a single motor (33,38).

CONCLUSIONS

Here we show by single-molecule imaging that a myoVa motor can processively transport cargo, in this case a Qdot, within a cell with stepping dynamics similar to that observed in vitro. However, it remains unclear how a myoVa undergoing a random walk along the cytoskeleton can deliver cargo effectively to destinations near the cell periphery. It should be noted that with TIRF imaging, the myoVa trajectories are observed only within the actin cytoskeleton that resides ~150 nm beneath the cell membrane. The rarity of Qdots departing the evanescent field and returning to the cell interior while moving several microns within the plane of the cell membrane suggests that the Qdot:myoVa conjugates were essentially at their destination. Perhaps their random paths might have been expected since the Qdots do not possess the necessary accessory proteins to target the cargo to its destination (39). However, provided that there is a component of myoVa processive movement within the trajectory, and that the overall orientation of actin network is such that the actin filament's barbed ends are pointed toward the periphery (40), the myoVa transporters should ultimately be able to deliver their cargo to destinations near the cell membrane.

Using the approach described here, it may be possible in future studies to characterize the targeting of motors to cargo in real time, as well as to determine how a given motor switches between actively transporting its cargo to being a passenger on the same cargo. Such studies, in combination with attempts to reconstruct an in vitro cytoskeleton in three dimensions, will ensure that significant progress can be made in understanding the complex nature of intracellular cargo transport.

SUPPORTING MATERIAL

Four figures, five movies, and references are available at http://www.biophysj.org/biophysj/supplemental/S0006-3495(09)00968-0.

The authors thank Guy Kennedy for optomechanical support, Sam Walcott for implementing the step-finding algorithm kindly provided by Jacob Kerssemakers and Marileen Dogterom, Samantha Previs for technical expertise, and Dimitry Krementsov and Marcus Thali for tissue culture assistance.

This work was supported by grants from the National Institutes of Health (HL007944 to S.R.N., GM078097 to K.M.T., and HL059408 to D.M.W.).

REFERENCES

1. Huang, J. D., S. T. Brady, B. W. Richards, D. Stenolen, J. H. Resau, et al. 1999. Direct interaction of microtubule- and actin-based transport motors. *Nature*. 397:267–270.
2. Kural, C., A. S. Serpinskaya, Y. H. Chou, R. D. Goldman, V. I. Gelfand, et al. 2007. Tracking melanosomes inside a cell to study molecular motors and their interaction. *Proc. Natl. Acad. Sci. USA*. 104:5378–5382.
3. Brown, J. R., P. Stafford, and G. M. Langford. 2004. Short-range axonal/dendritic transport by myosin-V: a model for vesicle delivery to the synapse. *J. Neurobiol*. 58:175–188.
4. Ali, M. Y., E. B. Krementsova, G. G. Kennedy, R. Mahaffy, T. D. Pollard, et al. 2007. Myosin Va maneuvers through actin intersections and diffuses along microtubules. *Proc. Natl. Acad. Sci. USA*. 104:4332–4336.
5. Ali, M. Y., H. Lu, C. S. Bookwalter, D. M. Warshaw, and K. M. Trybus. 2008. Myosin V and kinesin act as tethers to enhance each other's processivity. *Proc. Natl. Acad. Sci. USA*. 105:4691–4696.
6. Yildiz, A., J. N. Forkey, S. A. McKinney, T. Ha, Y. E. Goldman, et al. 2003. Myosin V walks hand-over-hand: single fluorophore imaging with 1.5-nm localization. *Science*. 300:2061–2065.
7. Warshaw, D. M., G. G. Kennedy, S. S. Work, E. B. Krementsova, S. Beck, et al. 2005. Differential labeling of myosin V heads with quantum dots allows direct visualization of hand-over-hand processivity. *Biophys. J*. 88:L30–L32.
8. Kural, C., H. Kim, S. Syed, G. Goshima, V. I. Gelfand, et al. 2005. Kinesin and dynein move a peroxisome in vivo: a tug-of-war or coordinated movement? *Science*. 308:1469–1472.
9. Nan, X., P. A. Sims, P. Chen, and X. S. Xie. 2005. Observation of individual microtubule motor steps in living cells with endocytosed quantum dots. *J. Phys. Chem*. 109:24220–24224.
10. Watanabe, T. M., and H. Higuchi. 2007. Stepwise movements in vesicle transport of HER2 by motor proteins in living cells. *Biophys. J*. 92:4109–4120.
11. Levi, V., V. I. Gelfand, A. S. Serpinskaya, and E. Gratton. 2006. Melanosomes transported by myosin-V in *Xenopus* melanophores perform slow 35 nm steps. *Biophys. J*. 90:L07–L09.
12. Mehta, A. D., R. S. Rock, M. Rief, J. A. Spudich, M. S. Mooseker, et al. 1999. Myosin-V is a processive actin-based motor. *Nature*. 400:590–593.
13. Veigel, C., F. Wang, M. L. Bartoo, J. R. Sellers, and J. E. Molloy. 2002. The gated gait of the processive molecular motor, myosin V. *Nat. Cell Biol*. 4:59–65.
14. Gross, S. P., M. C. Tuma, S. W. Deacon, A. S. Serpinskaya, A. R. Reilein, et al. 2002. Interactions and regulation of molecular motors in *Xenopus* melanophores. *J. Cell Biol*. 156:855–865.
15. Dubertret, B., P. Skourides, D. J. Norris, V. Noireaux, A. H. Brivanlou, et al. 2002. In vivo imaging of quantum dots encapsulated in phospholipid micelles. *Science*. 298:1759–1762.
16. Hodges, A. R., E. B. Krementsova, and K. M. Trybus. 2007. Engineering the processive run length of myosin V. *J. Biol. Chem*. 282:27192–27197.
17. Krementsov, D. N., E. B. Krementsova, and K. M. Trybus. 2004. Myosin V: regulation by calcium, calmodulin, and the tail domain. *J. Cell Biol*. 164:877–886.
18. Okada, C. Y., and M. Rechsteiner. 1982. Introduction of macromolecules into cultured mammalian cells by osmotic lysis of pinocytic vesicles. *Cell*. 29:33–41.

19. Courty, S., C. Luccardini, Y. Bellaiche, G. Cappello, and M. Dahan. 2006. Tracking individual kinesin motors in living cells using single quantum-dot imaging. *Nano Lett.* 6:1491–1495.

20. Sage, D., F. R. Neumann, F. Hediger, S. M. Gasser, and M. Unser. 2005. Automatic tracking of individual fluorescence particles: application to the study of chromosome dynamics. *IEEE Trans. Image Process.* 14:1372–1383.

21. Weihs, D., M. A. Teitell, and T. G. Mason. 2007. Simulations of complex particle transport in heterogeneous active liquids. *Microfluid Nanofluidics.* 3:227–237.

22. Saxton, M. J. 1997. Single particle tracking: the distribution of diffusion coefficients. *Biophys. J.* 72:1744–1753.

23. Kerssemakers, J. W., E. L. Munteanu, L. Laan, T. L. Noetzel, M. E. Janson, et al. 2006. Assembly dynamics of microtubules at molecular resolution. *Nature.* 442:709–712.

24. Kad, N. M., K. M. Trybus, and D. M. Warshaw. 2008. Load and Pi control flux through the branched kinetic cycle of myosin V. *J. Biol. Chem.* 283:17477–17484.

25. Press, W. H., S. A. Teukolsky, W. T. Vetterling, and B. P. Flannery. 1992. Numerical Recipes in C: The Art of Scientific Computing. Cambridge University Press, Cambridge, UK.

26. Griscelli, C., A. Durandy, D. Guy-Grand, F. Daguillard, C. Herzog, et al. 1978. A syndrome associating partial albinism and immunodeficiency. *Am. J. Med.* 65:691–702.

27. Pastural, E., F. J. Barrat, R. Dufourcq-Lagelouse, S. Certain, O. Sanal, et al. 1997. Griscelli disease maps to chromosome 15q21 and is associated with mutations in the myosin-Va gene. *Nat. Genet.* 16:289–292.

28. Svitkina, T. M., A. B. Verkhovsky, and G. G. Borisy. 1995. Improved procedures for electron microscopic visualization of the cytoskeleton of cultured cells. *J. Struct. Biol.* 115:290–303.

29. Caspi, A., R. Granek, and M. Elbaum. 2000. Enhanced diffusion in active intracellular transport. *Phys. Rev. Lett.* 85:5655–5658.

30. De La Cruz, E. M., A. L. Wells, S. S. Rosenfeld, E. M. Ostap, and H. L. Sweeney. 1999. The kinetic mechanism of myosin V. *Proc. Natl. Acad. Sci. USA.* 96:13726–13731.

31. Rosenfeld, S. S., and H. L. Sweeney. 2004. A model of myosin V processivity. *J. Biol. Chem.* 279:40100–40111.

32. Snider, J., F. Lin, N. Zahedi, V. Rodionov, C. C. Yu, et al. 2004. Intracellular actin-based transport: how far you go depends on how often you switch. *Proc. Natl. Acad. Sci. USA.* 101:13204–13209.

33. Yoo, J., T. Kambara, K. Gonda, and H. Higuchi. 2008. Intracellular imaging of targeted proteins labeled with quantum dots. *Exp. Cell Res.* 314:3563–3569.

34. Shubeita, G. T., S. L. Tran, J. Xu, M. Vershinin, S. Cermelli, et al. 2008. Consequences of motor copy number on the intracellular transport of kinesin-1-driven lipid droplets. *Cell.* 135:1098–1107.

35. Kulic, I. M., A. E. Brown, H. Kim, C. Kural, B. Blehm, et al. 2008. The role of microtubule movement in bidirectional organelle transport. *Proc. Natl. Acad. Sci. USA.* 105:10011–10016.

36. Brangwynne, C. P., G. H. Koenderink, F. C. MacKintosh, and D. A. Weitz. 2008. Cytoplasmic diffusion: molecular motors mix it up. *J. Cell Biol.* 183:583–587.

37. Luby-Phelps, K. 2000. Cytoarchitecture and physical properties of cytoplasm: volume, viscosity, diffusion, intracellular surface area. *Int. Rev. Cytol.* 192:189–221.

38. Cai, D., K. J. Verhey, and E. Meyhöfer. 2007. Tracking single kinesin molecules in the cytoplasm of mammalian cells. *Biophys. J.* 92:4137–4144.

39. Desnos, C., S. Huet, and F. Darchen. 2007. 'Should I stay or should I go?': myosin V function in organelle trafficking. *Biol. Cell.* 99:411–423.

40. Svitkina, T. M., A. B. Verkhovsky, K. M. McQuade, and G. G. Borisy. 1997. Analysis of the actin-myosin II system in fish epidermal keratocytes: mechanism of cell body translocation. *J. Cell Biol.* 139:397–415.